Excision methods for high resolution shock capturing schemes applied to general relativistic hydrodynamics

Ian Hawke,[1,2] Frank Löffler,[1] and Andrea Nerozzi[3,4]

[1] *Max-Planck-Institut für Gravitationsphysik, Albert-Einstein-Institut, 14476 Golm, Germany*
[2] *School of Mathematics, University of Southampton, Southampton SO17 1BJ, UK*
[3] *Institute of Cosmology and Gravitation, Mercantile House, Hampshire Terrace, PO1 2EG, Portsmouth UK*
[4] *Center for Relativity, University of Texas at Austin, Austin TX 78712-1081, USA*

(Dated: January 18, 2005)

We present a simple method for applying excision boundary conditions for the relativistic Euler equations. This method depends on the use of Reconstruction-Evolution methods, a standard class of HRSC methods. We test three different reconstruction schemes, namely TVD, PPM and ENO. The method does not require that the coordinate system is adapted to the excision boundary. We demonstrate the effectiveness of our method using tests containing discontinuites, static test-fluid solutions with black holes, and full dynamical collapse of a neutron star to a black hole. A modified PPM scheme is introduced because of problems arisen when matching excision with the original PPM reconstruction scheme.

PACS numbers: 02.70.Bf, 04.25.Dm, 04.30.Db, 95.30.Lz, 97.60.Lf

I. INTRODUCTION

With gravitational wave detectors such as LIGO, VIRGO and GEO operational the problem of calculating gravitational wave templates has become even more urgent. Amongst the physical models that are the best candidates for producing detectable wave signals those including highly relativistic matter near black holes stand out. In cases such as black hole / neutron star binaries, binary neutron star systems that collapse promptly to a black hole, accretion flows onto black holes and many models for gamma-ray bursts, detailed numerical simulations will be required to find the impact of varying physical parameters on the gravitational waves produced.

Black hole / neutron star binaries are on astrophysical grounds believed to be as likely as binary neutron star mergers, with expected event rates of one per year in a sphere of about 70 Mpc radius [1]. While signals from binary neutron stars are expected to give us information about the masses, spins and locations of the objects, they are not expected to give information about the internal structure of the stars. Signals from mixed binary systems, on the other hand, will provide information about the neutron star structure and equation of state (EOS) [2].

The crucial problem for numerical simulations involving 3D general relativity which must be overcome to simulate such physical systems is stability. With current formulations of the vacuum Einstein equations it is possible to produce long term simulations of black holes in certain situations [3, 4, 5]. These simulations typically require some part of the computational domain inside the black hole to be *excised*, with an inner boundary condition placed on a surface inside the apparent horizon. This apparent horizon is never outside the event horizon. Because no physical signal can travel outwards from such an horizon, excising the interior (or parts of it) should not affect the exterior spacetime, which is the only region we can observe. The main reason to excise the part of the spacetime containing the singularity is that otherwise steep gradients near the physical singularity form, which numerical codes cannot handle. The only long term stable simulations including black holes performed without excision [6, 7] use techniques that are only applicable when the black hole is present in the initial slice.

In contrast most simulations including hydrodynamics have either been performed on a fixed spacetime background, or have only been run until a short time after the formation of the black hole [8]. There have been fully dynamical simulations of matter with black holes in axisymmetry such as [9], but few in 3D [10, 11, 12].

In this paper we will present a simple method for excision boundaries applied to hydrodynamics. The boundary condition is based on High–Resolution Shock–Capturing (HRSC) methods which may be used in a hydrodynamics code, and theoretically could be applied to any system using such HRSC methods. We show how it can be applied to three different, standard reconstruction schemes: TVD, ENO and PPM. Because of some problems found using this boundary condition with the PPM scheme we introduce a modified version of PPM (MPPM), which solves these problems. This excision method, combined with a suitable excision method for the spacetime, allows long term simulations of matter in black hole spacetimes. This has been shown e.g. using our hydrodynamics code called `Whisky` in [10].

The outline of this paper is as follows. In section II and III respectively we outline the equations and HRSC methods that will be used. The modifications required at excision boundaries are given in section IV. Section V contains the tests used to validate the boundary conditions. Throughout this paper we shall use geometric units where $c = G = M_\odot = 1$. Greek indices are taken to run from 0 to 3, latin indices from 1 to 3. We adopt the standard convention for the summation over repeated indices. In section III latin indices denote the cell index.

II. MODEL AND EQUATIONS

We are interested in simulating hydrodynamical flows near black holes, so we use the equations of general relativistic hydrodynamics coupled to a dynamical spacetime, described by full general relativity. We use the flux-conservative Valencia 3+1 formulation of the hydrodynamical equations [13, 14, 15]. Although the results of Lax and Wendroff [16] show that if the scheme converges then it will converge to one of the (possibly infinitely many) weak solutions of the system of equations, the use of the correct conservation law form is known to be crucial as the results of Hou and Lefloch [17] show that a non-conservative scheme will *generically* converge to the wrong weak solution. The stress energy tensor is written as

$$T_{\mu\nu} = \rho h u_\mu u_\nu + p g_{\mu\nu}, \tag{2.1}$$

where ρ is the mass density of the fluid, $h = 1 + \epsilon + p/\rho$ the specific enthalpy with ϵ the specific internal energy, and p the pressure. u_μ is the 4-velocity of the fluid and $g_{\mu\nu}$ the 4-metric of the spacetime.

The equations of relativistic hydrodynamics can then be written in a conserved form

$$\partial_t \mathbf{q} + \partial_j \mathbf{f}^{(j)}(\mathbf{q}) = \mathbf{s}(\mathbf{q}). \tag{2.2}$$

Here we use the Valencia form [13, 14] as in [10, 18, 19]. The $\mathbf{q}$ is a vector of conserved variables. They are not strictly conserved because of the source terms $\mathbf{s}$, but in flat space the sources $\mathbf{s}$ vanish.

The system requires an EOS to close it. This is normally given by specifying the pressure p in the form $p = p(\rho, \epsilon)$. In this paper we will consider the standard perfect fluid gamma-law EOS

$$p = (\Gamma - 1)\rho\epsilon, \tag{2.3}$$

and often we will restrict to the polytropic EOS

$$p = K\rho^\Gamma, \tag{2.4}$$

which is a good approximation to neutron star matter in a cold neutron star and in the absence of shocks.

III. NUMERICAL METHODS

The numerical methods that we use for the evolutions of the hydrodynamic variables are all High–Resolution Shock–Capturing (HRSC) methods. We take the semidiscrete or method of lines reconstruction-evolution viewpoint: a piecewise continuous interpolant (the *reconstruction*) of each variable is found, at each cell boundary a Riemann problem is solved (usually approximately), the time derivative for each variable is constructed from the flux differences through the boundaries of each cell and the source terms are calculated, and the solution at the new timelevel is found using some suitable time integrator.

In what follows we shall specialise to the case of a uniform Cartesian grid.

A. Riemann solvers

Our code implements three independent approximate Riemann solvers (HLLE, Roe, modified Marquina). Although an integral part of the full HRSC method they are irrelevant for the problem of excision, as explained below. The Riemann solver employed in all tests shown below is the modified Marquina solver described in [20, 21].

B. Reconstruction methods

Four separate reconstruction methods are considered here. Each are applied in a dimensionally split fashion; the reconstructions are performed along each coordinate axis in turn. Although some of the reconstruction methods considered here have formal orders of accuracy that are better than second order, the formal global order of accuracy of the code is at best second order. This is due to the extension to multiple dimensions and the coupling to the spacetime. The flux through the cell boundary is approximated by the flux through the point in the middle of the cell boundary, using the reconstructed fluid variables and a second order approximation of the metric terms. The use of reconstruction methods that have one dimensional formal orders of accuracy better than second order leads to improvements in actual accuracy but not in the formal convergence order.

The method with the lowest formal order of accuracy is a slope limited total variation diminishing (TVD) method. The essentially non-oscillatory (ENO) methods may have extremely high orders of accuracy and are more accurate in absolute terms than TVD. However, it is often more efficient to use the piecewise-parabolic method (PPM) even though it only has at most third–order accuracy. The fourth method is a variant of PPM, and it is introduced for the first time here. It solves some problems found using PPM near the excision region. Therefore we call it MPPM for 'modified PPM'.

For conventions about subscripts and superscripts to denote cells, cell boundaries and left or right sided cell boundary values also see Fig. 1.

1. *Slope–limited TVD*

Total variation diminishing (TVD) methods as given by, e.g., [22], ensure that the solution remains monotonic to avoid spurious oscillations near discontinuities. In the case of slope-limited TVD the reconstruction is given by an average of a first–order and a second–order reconstruction. To reconstruct the variable q in the cell centred at

x_i two local "slopes" are defined,

$$\begin{aligned} \Delta_i^- &\equiv q_i - q_{i-1}, \\ \Delta_i^+ &\equiv q_{i+1} - q_i, \end{aligned} \tag{3.1}$$

which are then averaged to get the slope in the cell $\bar{\Delta}_i = (\Delta_i^- + \Delta_i^+)/2$. This slope is then multiplied by a *limiter* which is a function ϕ of the local slopes $\phi = \phi(\Delta_i^-, \Delta_i^+)$. This *limited slope* $\bar{\Delta}_i$ then gives the cell boundary data by

$$q_{i\pm 1/2} = q_i \pm \frac{1}{2}\bar{\Delta}_i. \tag{3.2}$$

If the slopes are not limited (i.e., the limiter $\phi = 1$) then the method is second order accurate. However, in the presence of steep gradients or discontinuities such a reconstruction will be oscillatory due to Gibb's effects. In these regions the limiter reduces the slopes to avoid overshoots, retaining monotonicity of the reconstruction.

2. ENO

The ENO methods of Harten et al. [23] are a very general class of methods. Here we only consider the simple ENO reconstruction of the variables as given by Shu in [24]. This provides arbitrary order of accuracy in space.

As in the TVD case, ENO reconstructions are cell based. The p^{th} order reconstruction compares all possible polynomial stencils of size p containing the cell to be reconstructed. The "least oscillatory" stencil is chosen by minimizing the absolute values of the divided differences that make up the stencil.

Let p be the order of the reconstruction. Suppose we are reconstructing the scalar function q in cell i. We start with the cell i. We then add to the stencil cell j, where $j = i \pm 1$, where we choose j to minimize the Newton undivided differences

$$q\left[i-1, i\right] \equiv q_i - q_{i-1}, \tag{3.3a}$$

$$q\left[i, i+1\right] \equiv q_{i+1} - q_i. \tag{3.3b}$$

We then recursively add more cells, minimizing the higher order Newton divided differences $q\left[i-1, \ldots, i+j\right]$ defined by

$$\begin{aligned} q\left[i-1, \ldots, i+j\right] = {} & q\left[i, \ldots, i+j\right] - \\ & q\left[i-1, \ldots, i+j-1\right]. \end{aligned} \tag{3.4}$$

The reconstruction at the cell boundary is given by a standard p^{th} order polynomial interpolation on the chosen stencil.

Shu [24] has outlined an elegant way of calculating the cell boundary values solely in terms of the stencil and the known data. If the stencil is given by

$$S(i) = \left\{i - r, \ldots, i + p - r - 1\right\}, \tag{3.5}$$

for some integer r, then there exist constants c_{rj} depending only on the grid x_i such that the boundary values for cell I_i are given by

$$\begin{aligned} q_{i+1/2} &= \textstyle\sum_{j=0}^{p-1} c_{r,j} q_{i-r+j}, \\ q_{i-1/2} &= \textstyle\sum_{j=0}^{p-1} c_{r-1,j} q_{i-r+j}. \end{aligned} \tag{3.6}$$

The constants $c_{r,j}$ are given by the rather complicated formula

$$c_{r,j} = \left\{ \sum_{m=j+1}^{p} \frac{\sum_{l=0, l\neq m}^{p} \prod_{q=0, q\neq m, l}^{p} \left(x_{i+1/2} - x_{i-r+q-1/2}\right)}{\prod_{l=0, l\neq m}^{p} \left(x_{i-r+m-1/2} - x_{i-r+L-1/2}\right)} \right\} \Delta x_{i-r+j}. \tag{3.7}$$

This calculation simplifies considerably if the grid is evenly spaced. For this case the coefficients up to seventh–order are given by Shu [24].

3. PPM

The Piecewise Parabolic Method (PPM) of Colella and Woodward [25], generalized to relativistic flows by Martí and Müller [26], is third–order accurate in space with particular special cases to ensure monotonicity at shocks, sharpening of contact discontinuities, and shock detection.

The outline of the general PPM method is as follows. The first step is to interpolate a quartic polynomial to the cell boundary,

$$q_{i+1/2} = \frac{1}{2}\left(q_{i+1} + q_i\right) + \frac{1}{6}\left(\delta_m q_i - \delta_m q_{i+1}\right), \tag{3.8}$$

where

$$\delta_m q_i = \begin{cases} \min(|q_{i+1}-q_{i-1}|, 2|q_{i+1}-q_i|, 2|q_i-q_{i-1}|)\ \mathrm{sign}(q_{i+1}-q_{i-1}) & \text{if } (q_{i+1}-q_i)(q_i-q_{i-1})>0 \\ 0 & \text{otherwise} \end{cases}. \tag{3.9}$$

At this point we set both left and right states at the interface to be equal to the interpolated value,

$$q^+_{i+1/2} = q^-_{i+1/2} = q_{i+1/2}. \tag{3.10}$$

This reconstruction will be oscillatory near shocks. Before a step which will preserve the monotonicity there are two other steps, which may be applied.

Firstly we may "steepen" discontinuities. This is to produce sharper profiles and is only applied to discontinuities that are mostly a contact (see [25] for the details). This procedure replaces the cell boundary reconstructions of the density with

$$\rho^+_{i-1/2} \equiv \rho^+_{i-1/2}(1-\eta) + \left(\rho_{i-1} + \frac{1}{2}\delta_m\rho_{i-1}\right)\eta, \tag{3.11a}$$

$$\rho^-_{i+1/2} \equiv \rho^-_{i+1/2}(1-\eta) + \left(\rho_{i+1} - \frac{1}{2}\delta_m\rho_{i+1}\right)\eta, \tag{3.11b}$$

where η is defined as

$$\eta \equiv \max\left[0, \min\left(1, \eta_1(\tilde{\eta}-\eta_2)\right)\right], \tag{3.12}$$

where η_1, η_2 are constants and

$$\tilde{\eta} \equiv \begin{cases} -\frac{1}{6}\frac{\rho_{i+2}-2\rho_{i+1}+2\rho_{i-1}-\rho_{i-2}}{\rho_{i+1}-\rho_{i-1}} & \text{if } -\delta^2\rho_{i+1}\delta^2\rho_{i-1}>0 \text{ and } |\rho_{i+1}-\rho_{i-1}| - \epsilon_S \min(|\rho_{i+1}|,|\rho_{i-1}|)>0 \\ 0 & \text{otherwise} \end{cases} \tag{3.13}$$

with ϵ_S another constant and

$$\delta^2\rho_i \equiv \rho_{i+1} - 2\rho_i + \rho_{i-1}. \tag{3.14}$$

Suggested values for the constants η_1, η_2 and ϵ_S can be found in [25].

Another step that may be performed before monotonicity enforcement is the "flattening" of the zone structure near shocks. This adds simple dissipation, altering the reconstructions to

$$q^+_{i-1/2} \equiv \nu_i q^+_{i-1/2} + (1-\nu_i)q_i, \tag{3.15}$$

$$q^-_{i+1/2} \equiv \nu_i q^-_{i+1/2} + (1-\nu_i)q_i, \tag{3.16}$$

where

$$\nu_i \equiv \begin{cases} \max\left[0, 1-\max\left(0, \omega_2\left(\frac{p_{i+1}-p_{i-1}}{p_{i+2}-p_{i-2}} - \omega_1\right)\right)\right] & \text{if } \epsilon\ \min(p_{i-1}, p_{i+1}) < p_{i+1}-p_{i-1} \text{ and } v^x_{i-1} - v^x_{i+1} > 0 \\ 1 & \text{otherwise} \end{cases}, \tag{3.17}$$

and ω_1, ω_2 and ϵ are again constants with suggested values given in [25]. Note that this step is a simplification

of the one in [25, 26], which reduces the communication overhead in parallel runs. No problems were encountered using this modification.

The final step is applied to preserve monotonicity, which prevents oscillatory reconstruction near shocks. The following replacements are made:

$$q^+_{i-1/2} \equiv q^-_{i+1/2} = q_i \quad \text{if } (q^-_{i+1/2} - q_i)(q_i - q^-_{i+1/2}) \le 0, \tag{3.18a}$$

$$q^+_{i-1/2} \equiv 3q_i - 2q^-_{i+1/2} \quad \text{if } (q^-_{i+1/2} - q^+_{i-1/2})\left(q_i - \frac{1}{2}(q^+_{i-1/2} + q^-_{i+1/2})\right) > \frac{1}{6}(q^-_{i+1/2} - q^+_{i-1/2})^2, \tag{3.18b}$$

$$q^-_{i+1/2} \equiv 3q_i - 2q^+_{i-1/2} \quad \text{if } (q^-_{i+1/2} - q^+_{i-1/2})\left(q_i - \frac{1}{2}(q^+_{i-1/2} + q^-_{i+1/2})\right) < -\frac{1}{6}(q^-_{i+1/2} - q^+_{i-1/2})^2. \tag{3.18c}$$

4. MPPM

As we shall see below there are situations where the PPM scheme does not give good results. This is due to the use of a fixed stencil in the first part of the PPM algorithm where the interpolated value is computed. This can cause problems with supersonic flows and when, as in our excision method, we try to match to a non-PPM method. To avoid this problem the modified PPM scheme changes the interpolated value in (3.8). The modified method uses the same steps as the PPM scheme after the interface values are set in Eq. (3.10) (discontinuity steepening, zone flattening and monotonicity preservation).

PPM uses the points at $i-1, i, i+1, i+2$ for the fourth order interpolation function to obtain a value at $i+\frac{1}{2}$. In the case of supersonic flow this centred stencil takes too much information from one side and too little from the other. Because of this, the method may produce small amplitude oscillations that are stable (due to the other steps in the PPM method) but which do not converge away. To cure this we need to use a stencil that depends on the data in some way.

In particular, we calculate the minimum and maximum characteristic velocities from the minimum and maximum eigenvalues λ_- and λ_+ of the Jacobian matrix $\partial\mathbf{f}/\partial\mathbf{q}$. Depending on these values, we define

$$\alpha = \frac{\lambda_- + \lambda_+}{|\lambda_-| + |\lambda_+|}, \tag{3.19}$$

which is a continuous function of the characteristic speeds that has value ± 1 whenever the flow is supersonic. Because the eigenvalues can only be in the range $[-1, 1]$ α is also in that range.

Using α we calculate the initial boundary states

$$q^+_{i+1/2} = \begin{cases} |\alpha|\, q_L + (1 - |\alpha|)\, q_{i+1/2}, & \text{if } \alpha < 0, \\ |\alpha|\, q_R + (1 - |\alpha|)\, q_{i+1/2}, & \text{if } \alpha > 0 \end{cases} \tag{3.20}$$

with

$$q_L = \frac{1}{12}\left(13q_{i+1} - 5q_{i+2} + q_{i+3} + 3q_i\right), \tag{3.21}$$

$$q_R = \frac{1}{12}\left(13q_i - 5q_{i-1} + q_{i-2} + 3q_{i+1}\right). \tag{3.22}$$

In this way we shift the stencil at most one cell to the side depending smoothly on the data. Note that this choice is arbitrary and could be chosen in a different way, but was sufficient for the tests used here. Because the value of the interpolating function at the boundary can be outside the range given by the values at the neighbouring cells q_i and q_{i+1}, we set the boundary values $q^+_{i+1/2}$ and $q^-_{i+1/2}$ in that case to be equal to the closest nearby cell value. Once the interpolated value is set we proceed as in the PPM case with the steps required to, e.g., preserve monotonicity, as given in Eqs. (3.11–3.18).

This procedure takes the characteristic speeds of the data into account and should therefore be more suitable to extreme cases where both minimal and maximal speeds have the same sign and are not close to zero. However, in cases with minimal and maximal characteristic speeds of the same size, but different sign, it should be as good as PPM.

IV. EXCISION BOUNDARIES

Excision boundaries are based on the principle that a closed region of spacetime that is causally disconnected from the rest of the simulated spacetime can be ignored without affecting the results in the exterior spacetime. A black hole event horizon is given indeed by the boundary of such a causally disconnected region of spacetime. As generically a curvature singularity will form within the horizon it will be necessary to remove it, and the associated steep gradients, from the numerical domain.

Excision boundaries are usually placed within a trapped surface such as an apparent horizon, as it is not possible to find the event horizon locally in time. We note that for a cubical region that is excised on a Cartesian grid to be a true trapped surface it may have to be placed well within the horizon, as pointed out by [27]. However, inflow boundary conditions applied to surfaces within the apparent horizon have been shown to work well [7].

The same considerations apply to the hydrodynamical variables as to the spacetime field variables. Again there

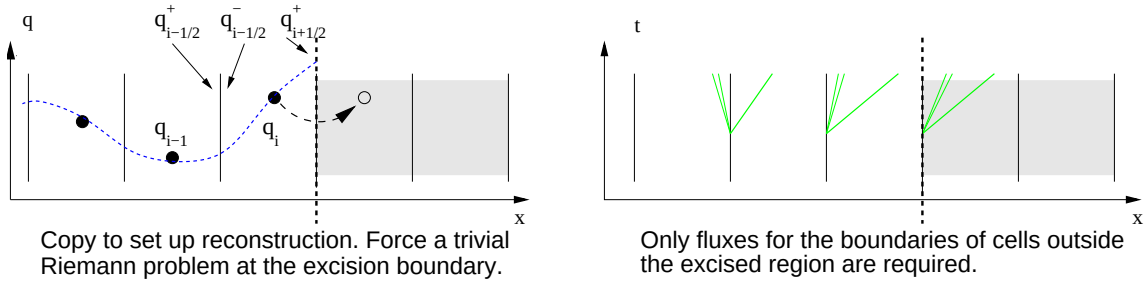

FIG. 1: A schematic view of the excision algorithm. The excised region is indicated by the shaded grey cells and the excision boundary by the vertical dotted line. In the left panel we indicate how the reconstruction method is modified near the excision boundary. The values required to compute the fluxes for the cell next to the boundary are indicated, along with the method used (simple copying) to "extend" the data across the excision boundary. Using this we can compute the fluxes through the cell boundaries for all cells outside the excised region. As shown in the right panel, these are the only fluxes required.

will be a region of spacetime in which the fluid is causally disconnected from the exterior. In practise due to the coupling with the spacetime field this will coincide with the event horizon as for the spacetime field. However, if the spacetime field variables have been excised then in principle there is no need to excise the hydrodynamical field variables at all, as these are not expected to blow up and form singularities independently of the spacetime field variables.

In practise unacceptable numerical errors are found if the hydrodynamical variables are not excised. In particular at typical resolutions it is possible for numerical effects in the interior of the black hole horizon to propagate out of the horizon through the hydrodynamical variables. Although we will exploit the independence *in principle* of the use of excision boundaries for the different field variables later, in practise both should be used simultaneously.

Excision boundary methods can be viewed in a number of different ways. Viewed at the level of the differential equations, all characteristics of physical quantities are going into the excision region. At the level of the Riemann problem, all possible waves from the solution of the Riemann problem must be contained within the excision region.

This immediately suggests a method that could be used at the excision boundary. As a HRSC method naturally changes the stencil locally depending on the data, we just need to guarantee that the data used to construct the flux at the excision boundary is the physically relevant data outside the excision region. This also suggests that the natural choice to put the excision boundary is not a cell centre, but a cell boundary.

While very simple, this method is not stable in general. It is equivalent to filling the first cell inside the excision region by linear extrapolation from the exterior (for a second–order HRSC method such as slope limited TVD reconstruction). This is not guaranteed to reduce the total variation of the solution, and so even simple examples do fail with this boundary condition.

On the other hand the simplest outflow boundary condition at the excision boundary does not have this problem. In particular, we may apply zero–order extrapolation (a simple copy) to all variables at the boundary to create data at the first cell inside the excision region. This is done for each of the three reconstruction methods. If one method requires more cells for the stencil in the interior of the excision region, we can then force the stencil to only consider the data in the first cell and the exterior as above.

A summary of our method is as follows:

1. Any point for which all possible reconstruction stencils are contained within the exterior spacetime (i.e., do not contain an excised point) is evolved in the normal fashion.

2. Any point which is contained within the excised region is not evolved at all.

3. All other points have at least one stencil that contains an excision point. To update these points we must reconstruct the data to both sides of each cell boundary. Once this is done the Riemann problem can be solved, the boundary flux found and the update computed. In order to reconstruct the data we do the following:

   (a) The values for all variables in the cell next to the excision boundary are copied to the first cell within the excision boundary.

   (b) A reconstruction of all cells is produced using only the data outside the excision region and the first cell within. The precise method depends on the global reconstruction method used and is explained below. In outline, the idea is to retain the order of accuracy by retaining the same size of the stencil if possible.

   (c) This method produces reconstructed data on both sides of every cell boundary *except* for the

excision boundary, where only the reconstruction from the exterior can be produced. At this boundary we assume on physical grounds that the solution of the Riemann problem must be given by the exterior state (as this is assumed to be an outflow boundary). Therefore at these points we do not solve the Riemann problem, but calculate the flux from the exterior reconstruction (see Fig. 1).

As an aside, we note that this means the method is independent of the choice of Riemann solver. However, the choice of a *trivial* Riemann problem at points that are not excised but where the reconstructed states are identical (e.g., in the atmosphere) can lead to gains in computational efficiency.

To completely describe our method in practice we just need to describe how the stencil is altered with the specific reconstruction methods we use. In what follows we consider a set of cells in one dimension. The coordinate is labelled x, the cell centres x_i, and the cell boundaries $x_{i\pm1/2}$ in an obvious notation. The excision boundary will be denoted $x_{B+1/2}$, with the cell x_{B+1} being excised. We want to calculate the update term for the cell centred at x_B by calculating the fluxes at $x_{B\pm1/2}$.

Excision of the spacetime variables is applied using the *simple lego* excision method described in, e.g., [3, 7].

1. Slope-limited TVD

In this case it is clear that only the reconstructions at $x_{B\pm1/2}$ are affected by the excision region. It is also clear that setting

$$\bar{\Delta}_B = \frac{1}{2}\left(\Delta_B^- + \Delta_B^+\right) = 0, \tag{4.1}$$

ensures that only data outside the excision region is used and is consistent with the TVD reconstruction.

2. ENO

As described in section III B 2 the ENO method uses a stencil width depending on the desired order of accuracy p. Hence the reconstruction in the cells centred between x_B and x_{B-p+2} are affected by the excision region.

It is clear how to ensure that the stencil chosen by the ENO reconstruction does not include any points from inside the excision region. The first divided differences that include points within the excision region are set to extremely large values with oscillating and growing amplitude such as $(-i)^i \times 10^{10}$ where i is the index of the cell ($i > 0$). The higher order divided differences are calculated from these, ensuring that the least oscillatory stencil does not include points from the excision region, but more points away from it. This is a simple application of the principle outlined by Shu [24] for dealing with outflow boundaries with ENO methods.

3. PPM

PPM uses a point stencil of five points, but reconstructs around a cell boundary instead of in a cell. Hence the reconstructions affected by the excision region are the reconstruction at left edge of $x_{B+1/2}$ and both reconstructions at $x_{B-1/2}$.

We have not attempted to find a consistent third–order reconstruction for these points. Instead we use the identical reconstruction as in the TVD case of section III B 1. As this provides a second–order stable reconstruction at an outflow boundary it does not affect the order of accuracy in the rest of the domain.

4. MPPM

Since excision should only be applied on a boundary with only outgoing characteristics, α should only be -1 or 1 depending on the direction of the boundary. Because of the symmetry of the cases, without loss of generality we assume $\alpha = 1$ from here on, that is assuming the excision boundary to be to the right of the computational domain.

In the case $\alpha = 1$ we effectively use a stencil with one point to the right and three points to the left instead of the usual symmetric four point stencil of the interpolation step of PPM. Because of this, we can use the usual MPPM procedure in the whole domain except for only one point next to the excision boundary. There we set the left and right boundary values to be the cell value as in the TVD case.

V. NUMERICAL TESTS

In this Section we present some simple numerical tests to validate our approach. The results were calculated using the Whisky code [10]. Where the spacetime was evolved an implementation [28, 29] of the NOK (BSSN) formulation of [30, 31] was used, with the excision method given in [3]. Apparent horizons were found using the code described in [32] and event horizons using the code described in [33]. All codes use the Cactus framework [34].

A. Shock wave tests

Special relativistic shock tubes are the simplest possible test. For this test the spacetime background is fixed to be Minkowski spacetime in standard coordinates. It is simple to choose initial data such that the chosen excision boundary is an outflow boundary for all time. In particular, we are using initial data in which $\rho_L = 10$, $\rho_R = 1$, $v_L = v_R = 0$, $p_L = 40/3$ and $p_R = 2/3 \times 10^{-6}$ and the velocity is normal to the interface. The ideal fluid equation of state, Eq. (2.3), is used, with $\Gamma = 5/3$.

We have considered three different cases. The first and simplest was a shock aligned with a coordinate axis with the excision boundary normal to the shock. The second and numerically more complex was a shock along the diagonal of the 3D box with the excision boundary normal to the shock. The final test consisted of a shock not aligned with the grid and with the excision boundary given by a sphere. The test requires more care in setting the domain evolved as the excision boundary is no longer an outflow boundary over the entire spacetime, but only within a localized region. Here we set the domain such that the intersection of the excision boundary with the domain forms a hemisphere.

The results of the first test for PPM are shown as an example in Fig. 2. All methods give nearly the same results, are stable and for all methods the shock passes cleanly through the excision boundary, with the results matching the analytic solution well. All other tests showed similar results, with stable and accurate results independent of the relative geometry of the shock and excision boundary.

An example of what may go wrong with an incorrect excision boundary condition is shown in Fig. 3. Here the standard excision boundary condition presented in section IV is compared to an alternative method where the first point inside the excision region is set to very small values. The result is a stable evolution which is correct except for a few points near the boundary. Here the density overshoots except for the point nearest the boundary which itself drops to atmosphere values. Although in this simple test the boundary condition is inaccurate, but stable, this seems unlikely to remain the case in more complex situations. Other boundary conditions, such as first–order extrapolation to the first point within the excision region, fare even worse, as they actually fail to produce a stable evolution even on this simple test.

B. Michel solution

The Michel solution [35] is a stationary solution of spherical accretion onto a Schwarzschild black hole in the test fluid approximation. Here we will consider Eddington-Finkelstein coordinates so that the slice penetrates the horizon. This solution is often used to validate relativistic hydrodynamic codes [36, 37].

The solution is derived from the basic equations of mass and energy conservation for the fluid and is obtained numerically using a Newton–Raphson interation scheme.

The first three plots in Fig. 4 show a part of the results of a series of runs made to test the Michel solution. In these plots the ENO reconstruction method is used, but the graphs look very similar for TVD, PPM and MPPM. We set the Michel solution to be our initial data, then we evolve it and verify its accuracy. In the plot, the exact solution is compared with the computed solution at time $t = 40$ (in units of the background black hole mass). Using a logarithmic plot we show the results for the density, x-velocity and pressure. The two sets of data are in very good agreement, as expected from the staticity of the solution. It is possible to notice a slight discrepancy in the first grid point next to the excision region (dotted line). This discrepancy is related to the lower accuracy which we have there, visually amplified on the plot by the choice of logarithmic scale. This is the case for all reconstruction methods.

The fourth plot in Fig. 4 shows instead the convergence factor obtained for all the reconstruction methods on the same set of simulations. As evident in the figure, PPM does not show convergence, while the other reconstruction methods show the expected convergence factor of approximately two. We will discuss the possible reason for that later.

C. Neutron Star collapse

As the next test we consider the collapse of a neutron star, in a simulation in which both the spacetime and the matter are evolved. This test is considerably more difficult than previous tests, requiring both hydrodynamic fields and spacetime to be consistently excised, and requiring a dynamic excision region.

As in [19] a spherically symmetric polytrope with $K = 100$, $\Gamma = 2$ and a central density of $\rho_c = 8 \times 10^{-3} \approx 4.95 \times 10^{15}\,\mathrm{g\,cm^{-3}}$ is used. The collapse was induced by lowering K by 2% and rescaling the matter variables to enforce the solution of the constraints. Note that because this satisfies the constraints and the spacetime is not changed, the ADM mass of the system is also not changed by this.

Due to the symmetry of the problem we only evolve one octant of the grid. The spacetime is evolved using the NOK formulation and the excision methods described in [3, 4]. The apparent horizon, if it can be found, is located using the horizon finder described in [32]. The gauge conditions used are "1+log" slicing for the lapse and the gamma-driver condition given in equation (45) of [6]. The event horizon is located using the code described in [33].

In Fig. 5 we show the mass of the event and apparent horizons of the black hole found by measuring their surface areas and using $M = (A/16\pi)^{1/2}$ and the ADM mass computed by the inital data solver for comparison. At early times the expected results are seen: the mass of the apparent horizon is less than the mass of the event horizon which is less than the total ADM mass of the spacetime. At late times large violations of the Hamiltonian constraint develop, errors in the determination of the horizon become large and lead eventually to the crash of the code at around $t = 0.455$ms. Without excision the code crashes shortly after formation of the apparent horizon.

We believe that the origin of these instabilities lies in the spacetime excision technique, and not the hydrodynamic excision described here. This can be seen much

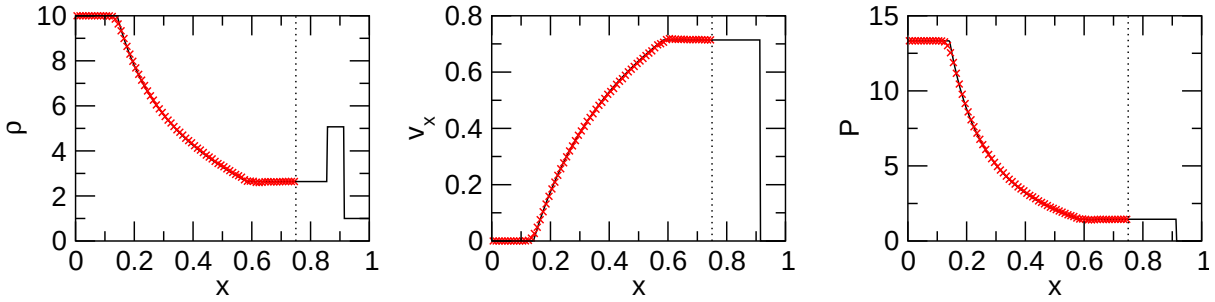

FIG. 2: A simple shock propagating parallel to the x axis hits an excision boundary normal to the x axis (dotted line). As expected, the shock is completely absorbed. The solid line is the exact solution, the crosses are the numerical solution for the PPM scheme. Plots of the other reconstruction methods show qualitatively the same behaviour. The time shown is $t = 0.5$.

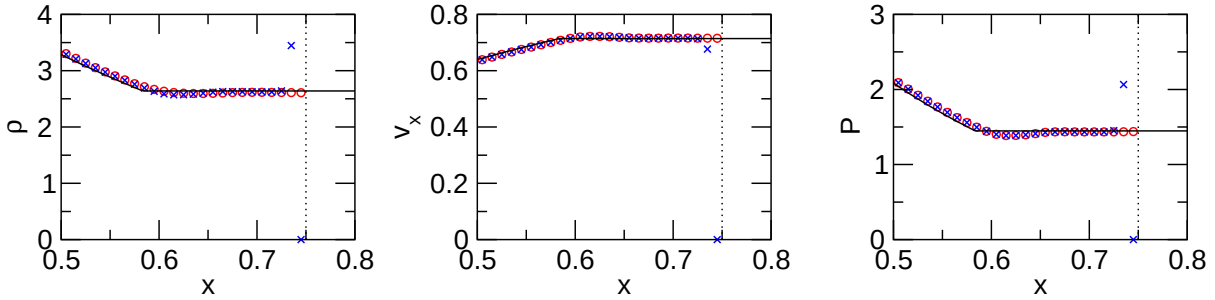

FIG. 3: As in Fig. 2, a shock is propagated parallel to the x axis through an excision boundary. In this case a non-conservative excision boundary condition is used. This excision boundary condition, which is based on setting all variables in the first excised cell to very small ("atmosphere") values gives inaccurate but stable results. The circles represent the stable and accurate numerical result found using the excision boundary method described in this paper.

more clearly in another test, where we used a slowly rotating neutron star (model D1 of [10]) and excise the spacetime variables and the matter variables at different times and compare the evolution of the 2-norm of the Hamiltonian constraint in the two cases. Note that it is not possible to first excise the spacetime variables and later the hydrodynamics because the hydrodynamics code is very sensitive to errors in the spacetime. Therefore we always first excise the hydrodynamical variables and then switch on the excision of the spacetime at a later time. We excise the hydrodynamic variables shortly after an apparent horizon is found (which in this case is at a *coordinate* time of 0.546ms) and vary the coordinate time, $t_{\rm ex}$, when the spacetime is first excised.

Figure 6 shows the Hamiltonian constraint violation for simulations where the excision time $t_{\rm ex}$ is varied. For comparison, a simulation where neither the hydrodynamical variables nor the spacetime variables were excised, and a simulation where only the hydrodynamical variables are excised, are also shown.

Where the hydrodynamical or spacetime variables are excised the Hamiltonian constraint violation inside the excised region is not taken into account. At the point where either set of variables is excised the constraints are clearly meaningless within the excision region. We expect this to have no effect on the exterior spacetime as demonstrated numerically in, e.g., [7]. The constraint violations in the exterior spacetime clearly are meaningful, and we will be most interested in the behaviour shortly after either set of variables is excised

It is clear that shortly after the time when the spacetime variables are excised there is a sudden exponential increase in the violation of the constraints. This does not happen at the time when the excision of the hydrodynamical variables first takes place. We believe this indicates that the cause of the instabilities encountered is the method used to excise the spacetime variables. Whilst we cannot rule out instabilities from the hydrodynamical excision, the simulation where only the hydrodynamical variables are excised seems to lose accuracy due to classical slice stretching effects and not due to the high frequency oscillations which are instead observed when excising the spacetime variables.

VI. CONCLUSION

Long term evolutions involving black holes and matter will require excision boundary conditions for the matter fields. For hydrodynamics, where the fluid will gener-

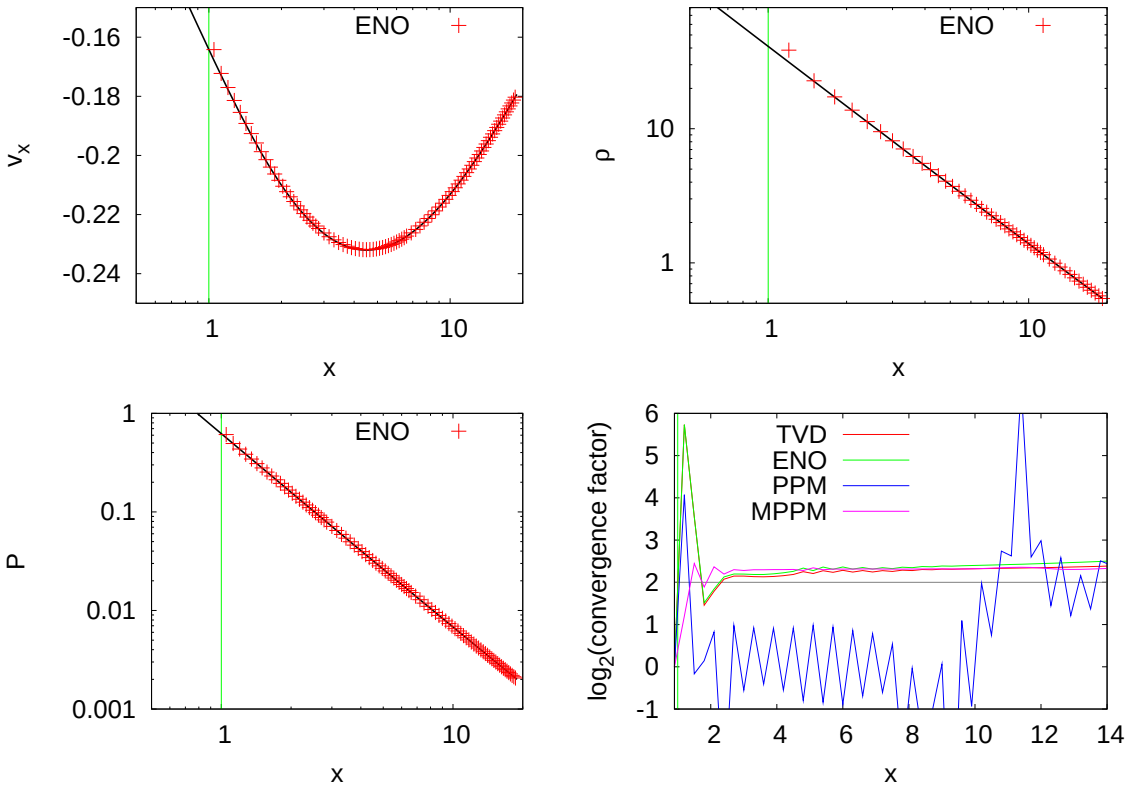

FIG. 4: Michel solution compared with the numerical evolution for the ENO method. All other methods look very similar in the physical quantities. The graphs show the values for the x component of the velocity v_x, the density ρ, and the pressure p of the fluid. Each quantity is evolved until time $t = 40$ (in units of the background black hole mass), and the numerical values are compared with the exact solution (the solid line in the graphs). The x axis is the radial distance expressed in black hole units. The excision region is delimited by the vertical, dotted line. The last graph shows the convergence factor of all reconstruction methods, where the expected second–order convergence is seen for all methods except for PPM.

ically form shock waves, the results of Lax and Wendroff [16] and Hou and Lefloch [17] imply that a conservative total-variation stable scheme must be used, which presently means a HRSC scheme. Although errors in the hydrodynamics at the excision boundary should not propagate outside of the horizon and so should have no effect on the physics, such inconsistencies may lead to numerical instabilities.

In this paper we have shown a simple method of providing a consistent excision boundary condition for systems of equations in conservation law form evolved with HRSC schemes. Although we have only applied this technique to the Valencia formulation of relativistic hydrodynamics [13, 14, 15] we expect the results to apply to any system where the conservation law form can be applied. The method is simple and works on a broad range of HRSC schemes.

The tests of section V show that the method works for shocks, steady state cases, and dynamical evolutions. The shock tests are particularly simple and enlightening, showing that an incorrect boundary condition may lead to inconsistency or numerical instabilities. The Michel solution test shows that our boundary conditions are also suited to long term steady state evolutions with strong gradients.

The dynamical collapse of a spherically symmetric TOV star shows the advantages and current limitations of our methods. The collapse to a black hole is accurately followed long past the formation of the horizon, the mass of which is computed to high accuracy. However, the simulation does not continue indefinitely, eventually failing due to a numerical instability. Simulations including rotation show the same features and, by varying the initial time at which excision is applied, there is evidence that the cause of the instabilities is the excision method applied to the spacetime variables, not the hydrodynamical method that is the focus of this paper. However we want to emphasise that although we believe that the simple lego excision boundary condition is the cause of the instabilities, the excision of the spacetime variables is nevertheless improving the length of the simlulations in the cases described here.

It has been suggested that HRSC methods may improve spacetime evolutions for certain hyperbolic formu-

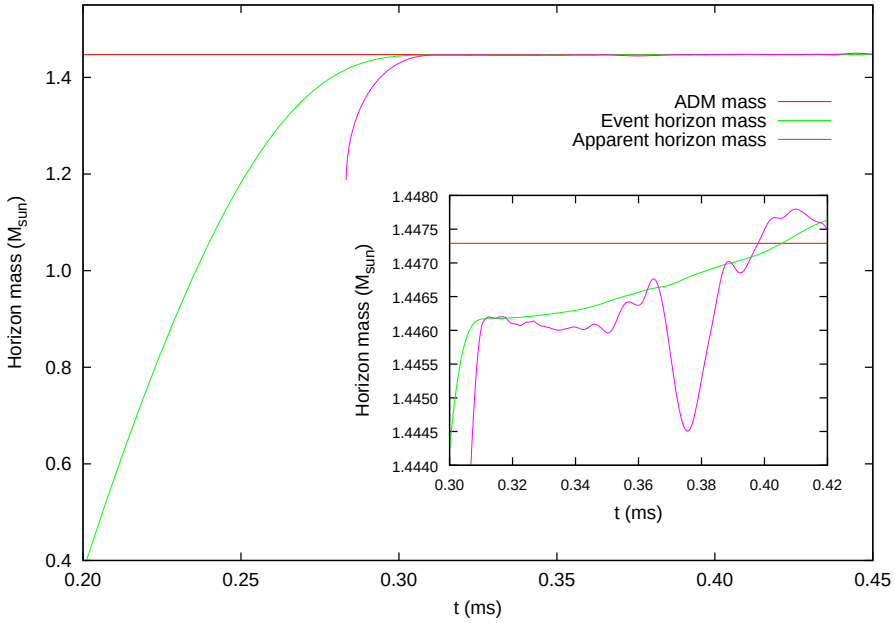

FIG. 5: Horizon masses for the collapse of a spherically symmetric neutron star. At early times the evolution is stable and accurate. The neutron star collapses smoothly into the horizon and the matter is excised. The horizon masses as measured by apparent and event horizon finders are very close to the total ADM mass of the initial spacetime, as expected. At late times instabilities lead to inaccuracies, as seen in the inset, before the simulation fails.

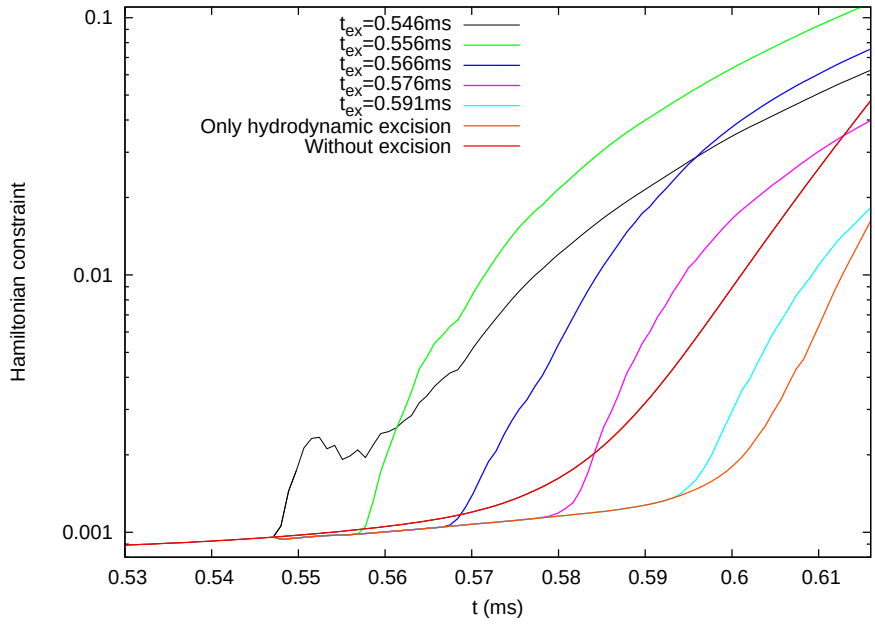

FIG. 6: The Hamiltonian constraint violation over time, plotted for different starting times $t_{\rm ex}$ of the spacetime excision. In every case (except the reference case where no excision is used) the hydrodynamical variables are excised as soon as the apparent horizon is found at $t = 0.547$ms. Instabilities at the excision boundary are believed to be the cause of the eventual failure of the simulation. Here it is clear that when the excision boundary condition is applied to the spacetime variables there is an immediate exponential growth in the constraint violation. In contrast, no growth is seen at the time when the hydrodynamical variables are excised. The instabilities which are indicated by the exponential growth of the constraint violations are clearly triggered by the spacetime excision.

lations of Einsteins Equations (e.g., [38, 39, 40]). If such a method were used, excision boundary conditions such as those presented in this paper should be easy to adapt. There are also other approaches to applying excision boundary conditions that show great promise (e.g., [41, 42, 43]). It is, however, not clear if these methods will work in situations where fundamental variables may become discontinuous. In such cases the methods presented here could then be used for a matter field where the evolution equations could be written in conservation law form, and any alternative method could be used for the spacetime.

At no point here we have addressed the question of the well-posedness of the system used, or any analytical proof of the stability of our method. The well-posedness of the simple Euler equations with arbitrary initial data in more than one dimension in the absence of gravity is not yet established; the most relevant current result ([44]) considers the one dimensional Euler equations on a plane-symmetric Gowdy spacetime. Given the current state of knowledge, and the successes in extending one-dimensional schemes that are known to be stable to more than one dimension, we expect that methods such as the one given here will be stable but are unable to give a proof at any level.

Acknowledgments

We want to thank all people involved in the effort of building the Whisky code, Jonathan Thornburg for his apparent horizon finder, Peter Diener for his event horizon finder and all people in the Cactus-code team for producing an efficient infrastructure for our work. We are also very grateful to Luciano Rezzolla and the people at the AEI for discussions and want to thank Luca Baiotti, Denis Pollney, Luciano Rezzolla, Ed Seidel and Jonathan Thornburg for proof-reading the manuscript. The simulations were performed on the peyote cluster at the AEI and an Origin 300 at Portsmouth, funded by a UK SRIF grant. IH was partially supported by PPARC grant PPA/G/S/2002/00531. AN was partly supported by NASA grant NNG04GL37G to the University of Texas at Austin.

[1] H. Bethe and G. Brown, Astroph. J. **506**, 780 (1998).
[2] M. Vallisneri, in *Proceedings of the 25th J. Hopkins Workshop on Current Problems in Particle Theory, 2001* (2002).
[3] M. Alcubierre and B. Brügmann, Phys. Rev. D **63**, 104006 (2001), gr-qc/0008067.
[4] M. Alcubierre, B. Brügmann, D. Pollney, E. Seidel, and R. Takahashi, Phys. Rev. D **64**, 061501(R) (2001), gr-qc/0104020.
[5] H.-J. Yo, T. W. Baumgarte, and S. L. Shapiro, Phys. Rev. D **66**, 084026 (2002).
[6] M. Alcubierre, B. Brügmann, P. Diener, M. Koppitz, D. Pollney, E. Seidel, and R. Takahashi, Phys. Rev. D **67**, 084023 (2003), gr-qc/0206072.
[7] M. Alcubierre, B. Brügmann, P. Diener, F. Herrmann, D. Pollney, E. Seidel, and R. Takahashi, submitted to Phys. Rev. D (2004), gr-qc/0411137.
[8] M. Shibata, Astrophys. J. **595**, 992 (2003), astro-ph/0310020.
[9] S. Brandt, J. A. Font, J. M. Ibáñez, J. Massó, and E. Seidel, Comp. Phys. Comm. **124**, 169 (2000).
[10] L. Baiotti, I. Hawke, P. J. Montero, F. Löffler, L. Rezzolla, N. Stergioulas, J. A. Font, and E. Seidel, Phys. Rev. D (2004), in press; gr-qc/0403029, gr-qc/0403029.
[11] M. D. Duez, S. L. Shapiro, and H.-J. Yo, Phys. Rev. D **69**, 104016 (2004), gr-qc/0401076.
[12] M. D. Duez, Y. T. Liu, S. L. Shapiro, and B. C. Stephens, Phys. Rev. D **69**, 104030 (2004), gr-qc/0402502.
[13] J. M. Martí, J. M. Ibánez, and J. M. Miralles, Phys. Rev. D **43**, 3794 (1991).
[14] F. Banyuls, J. A. Font, J. M. Ibánez, J. M. Martí, and J. A. Miralles, ApJ **476**, 221 (1997).
[15] J. Ibánez, M. Aloy, J. Font, J. Martí, J. Miralles, and J. Pons, in *Godunov methods: theory and applications*, edited by E. Toro (Kluwer Academic/Plenum Publishers, 2001).
[16] P. D. Lax and B. Wendroff, Comm. Pure Appl. Math. **13**, 217 (1960).
[17] T. Y. Hou and P. G. LeFloch, Math. of Comp. **62**, 497 (1994).
[18] J. A. Font, M. Miller, W. M. Suen, and M. Tobias, Phys. Rev. D **61**, 044011 (2000).
[19] J. A. Font, T. Goodale, I. Sai, M. Miller, L. Rezzolla, E. Seidel, N. Stergioulas, W. M. Suen, and M. Tobias, Phys. Rev. D **65**, 084024 (2002).
[20] M. A. Aloy, J. A. Pons, and J. M. Ibánez, Comput. Phys. Commun. **120**, 115 (1999).
[21] M. A. Aloy, J. M. Ibánez, J. M. Martí, and E. Müller, Astroph. J. Supp. **122**, 151 (1999).
[22] B. J. van Leer, Journal of Computational Physics **32**, 101 (1979).
[23] A. Harten, B. Engquist, S. Osher, and S. R. Chakrabarty, J. Comput. Phys. **71**, 2311 (1987).
[24] C. W. Shu, in *High-Order Methods for Computational Physics*, edited by T. J. Barth and H. Deconinck (Springer, 1999).
[25] P. Colella and P. R. Woodward, J. Comput. Phys. **54**, 174 (1984).
[26] J. M. Martí and E. Müller, J. Comput. Phys. **123**, 1 (1996).
[27] G. Calabrese, L. Lehner, D. Neilsen, J. Pullin, O. Reula, O. Sarbach, and M. Tiglio, Class. Quantum Grav. **20**, L245 (2003), gr-qc/0302072.
[28] M. Alcubierre, B. Brügmann, T. Dramlitsch, J. A. Font, P. Papadopoulos, E. Seidel, N. Stergioulas, and R. Takahashi, Phys. Rev. D **62**, 044034 (2000), gr-qc/0003071.
[29] M. Alcubierre, G. Allen, B. Brügmann, E. Seidel, and W.-M. Suen, Phys. Rev. D **62**, 124011 (2000), gr-

qc/9908079.
[30] M. Shibata and T. Nakamura, Phys. Rev. D **52**, 5428 (1995).
[31] T. W. Baumgarte and S. L. Shapiro, Phys. Rev. D **59**, 024007 (1999), gr-qc/9810065.
[32] J. Thornburg, Class. Quantum Grav. **21**, 743 (2004), gr-qc/0306056, URL `http://stacks.iop.org/0264-9381/21/743`.
[33] P. Diener, Class. Quantum Grav. **20**, 4901 (2003), gr-qc/0305039.
[34] Cactus, *http://www.cactuscode.org*.
[35] F. C. Michel, Astrophys. Spa. Sci. **15**, 153 (1972).
[36] P. Papadopoulos and J. A. Font, Phys. Rev. D **58**, 24005 (1998).
[37] J. A. Font and J. M. Ibánez, ApJ **494**, 297 (1998).
[38] C. Bona, J. Massó, E. Seidel, and J. Stela, Phys. Rev. Lett. **75**, 600 (1995), gr-qc/9412071.
[39] J. Bardeen and L. Buchman, Phys. Rev. D **65**, 064037 (2002).
[40] C. Bona, T. Ledvinka, C. Palenzuela-Luque, J. A. Pons, and M. Žáček (2004), gr-qc/04100799.
[41] G. Calabrese and D. Neilsen, Physical Review D **69**, 044020 (21 pages) (2004), gr-qc/0308008.
[42] G. Calabrese, L. Lehner, O. Reula, O. Sarbach, and M. Tiglio (2003), gr-qc/0308007.
[43] J. Thornburg, Class. Quantum Grav. **21**, 3665 (2004), gr-qc/0404059, URL `http://stacks.iop.org/0264-9381/21/3665`.
[44] A. P. Barnes, P. G. Lefloch, B. G. Schmidt, and J. M. Stewart, Classical and Quantum Gravity **21**, 5043 (2004).